THE UNIVERSITY OF

WARWICK

Modeling the evolution of natural cliffs subject to weathering: 2. Discrete element approach

S. Utili[1] and G. B. Crosta[2]

[1] The evolution of slopes subjected to weathering has been modeled by assuming Mohr-Coulomb behavior and by using a numerical approach based on the discrete element method (DEM). According to this method, soil and/or rock are represented by an assembly of bonded particles. Particle bonds are subject to progressive weakening, and so the material weathering and removal processes are modeled. Slope instability and material movement follow the decrease of material strength in space and time with the only assumption concerning the weathering distribution within the slope. First, the case of cliffs subject to strong erosion (weathering-limited conditions) and uniform weathering was studied to compare the results of the DEM approach with the limit analysis approach. Second, transport-limited slopes subject to nonuniform slope weathering were studied. Results have been compared with experimental data and other geomorphologic models from the literature (Fisher-Lehmann and Bakker–Le Heux). The flux of material from the slope is modeled assuming degradation both in space and time.

1. Introduction

[2] The evolution of hillslopes or scarps, formed by erosional, depositional or tectonic processes is strongly controlled by the physical mechanical properties, the mechanical behavior of the involved materials and their changes because of weathering, alteration, degradation. In absence of strong climatic changes, the climatic constrains can be considered stable and uniformly distributed over time. As a consequence, changes in physical and mechanical properties and mechanical behavior become the only constraints.

[3] Any geomaterial (e.g., granite, clay, shale, sandstone, chalk, pyroclastic deposits) [e.g., *Heimsath et al.*, 1997; *Dixon and Thorn*, 2005] can undergo degradation by weathering, alteration and progressive damage with different rate and at different depth and by different agents. Degradation of physical and mechanical properties can occur at the slope front, by soil and regolith production, but also well within the slope (e.g., by seepage and alteration, dissolution, suffusion). Weathering can influence both the cohesive and frictional part of the strength, with a more pronounced decrease in cohesion than friction.

[4] The progressive slope evolution through a series of mass movements (involving erosion, transport and deposition) has usually been recognized as a major problem in simulating slope development [e.g., *Kirkby*, 1987]. In fact, a particular failure can strongly influence both the subsequent slope geometry and the magnitude of the mass transfer through the entire length or a specific sector of the slope. Aggregated or long-term models are usually unsuitable for modeling this behavior because they suppress or redistribute the contribution of each major event. Furthermore, a sequence of successive slope failures along a cliff can be characterized by a change in size of the failing mass and of the time interval between successive failures.

[5] Classical diffusion-like models do not explicitly include the dynamic effects arising from the detachment of large masses which redistribute themselves differently along the lower part of the slopes. The same can be said for the protective action played by the debris on the underlying bedrock which is covered and isolated by the meteo-climatic agents.

[6] In the literature different models to study dynamic slope evolution with time can be found. *Fisher* [1866] analyzed the parallel retreat of coastal chalk cliffs accompanied by the accumulation of a basal debris apron. *Lehmann* [1933] extended Fisher's model by introducing the effect of different weathering stages. This model was further modified by *Bakker and Le Heux* [1946] and successively by other researchers ([e.g., *Nash*, 1981] introduced the effect of upper and lower sloping sectors). Later the diffusivity approach [see *Utili and Crosta*, 2011, and references therein] has been introduced.

[7] In this paper, first the discrete element method is introduced; second, the case of uniform weathering will be illustrated; and third, different hypotheses on nonuniform weathering will be introduced. Creep, slope wash, rain splash erosion and solute transport are not considered in

[1] Department of Engineering Science, University of Oxford, Oxford, UK.
[2] Dipartimento di Scienze Geologiche e Geotecnologie, Università degli Studi di Milano-Bicocca, Milan, Italy.
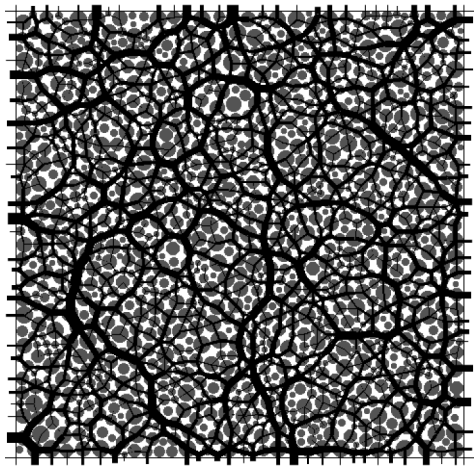
Figure 1. Specimen used for the DEM biaxial tests after completion of the generation procedure. The thickness of the black lines is proportional to the normal forces exchanged at contacts; disks are gray-colored.

this study. The study analyses slope evolution under weathering limited conditions, that is, more material can be transported than the one provided by degradation (weathering, alteration).

[8] The first case is introduced to compare the results obtained by the DEM with predictions by limit analysis (LA) [see *Utili and Crosta*, 2011]. In the second part, more hypotheses on weathering distribution within the slopes will be introduced and a comparison with relevant geomorphological models and examples will be carried out.

2. The DEM Approach

[9] A geomaterial can be seen as an assembly of spheroidal grains with frictional interfaces connected together by bonds. The discrete element method (DEM), which was introduced by *Cundall and Strack* [1979] to study the behavior of granular geomaterials, is a numerical procedure able to describe the mechanics of such an assembly. Appropriate parameters should be chosen to pass from micromechanical quantities (bond strength, interface friction and intergranular normal and shear compliances) to macroscopic mechanical properties, characterizing strength (e.g., friction and cohesion) and deformability (e.g., Young's modulus and Poisson's ratio) of the geomaterial.

[10] In the problems considered, the strength parameters are the relevant ones. *Utili* [2006] and *Utili and Nova* [2008] established a calibration procedure to connect the microscopic parameters of an assembly of 2-D discs of different sizes to its overall strength parameters in plane strain conditions. This procedure requires several biaxial tests to be carried out (see Figure 1). The particle radii distribution adopted was uniform between a minimum and maximum radius, R_{min} and R_{max} respectively, with $R_{max}/R_{min} = 3$ and $R_{min} = 1.48$ mm. Tests are repeated for different values of the "confining pressure." The resulting peak of the deviator stress is roughly proportional to the confining pressure. Then, an overall value of the friction angle (ϕ) of the granular material can be derived. This is in turn linearly related to the value of the friction angle at the contacts (ϕ_μ)

(see Figure 2). In order to obtain realistic values of overall friction, particle rotations were inhibited. This "unphysical assumption" can be justified as an indirect way of taking into account the interlocking effect due to the nonspherical shape of real particles. A linear relationship between ϕ_μ and ϕ was already found in 1994 by *Ng and Dobry* [1994] for a similar range of ϕ values. In that paper a detailed discussion about the effect of blocking particle rotations for a 2-D granular material can be found. The micromechanical strength parameters, (ϕ_μ, c_μ), were linked with the macromechanical ones (ϕ, c) by the following two relationships [*Utili and Nova*, 2008]:

$$\phi = K_1 \phi_\mu + K_2 \tag{1a}$$

$$c = \frac{K_3}{\left(\tan \phi_\mu\right)^{K_4}} c_\mu. \tag{1b}$$

The relationship between c and c_μ of equation (1b) is illustrated in Figure 3. Concerning the observed maximum dilation angle, it increases with increasing peak friction angle, decreasing confining pressure and increasing bond strength, c_μ. These trends are in agreement with other 2-D DEM analyses of bonded granulates [see *Wang and Leung*, 2008; *Jiang et al.*, 2010].

[11] To ensure faster convergence of the numerical process, *Cundall* [1987] introduced a damping force, modifying the Newton's law of dynamics as follows:

$$F_k - \xi|F_k|\text{sgn}(v_k) = ma_k, \tag{2}$$

where ξ is the damping coefficient, m is the particle mass, and v_k and a_k are the component of velocity and of acceleration for a particle, respectively (sgn (v_k) = 1 if $v_k > 0$, sgn (v_k) = −1 if $v_k < 0$, and sgn (v_k) = 0 if $v_k = 0$). If a significant damping force is used and dynamic simulations are run, an artificial energy dissipation is introduced causing a nonphysical slowing down of particles and unrealistic long runout times. However, in all the simulations a very small value of damping, 5%, was used. Moreover, it has been
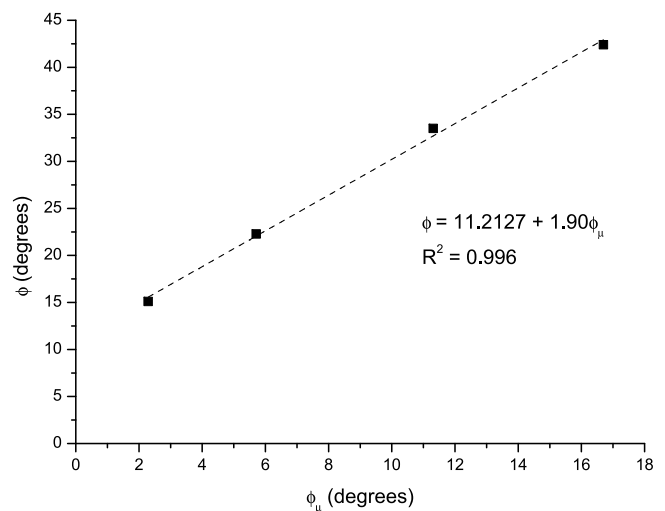

Figure 2. Macroscopic versus microscopic friction angle [after *Utili and Nova*, 2008].
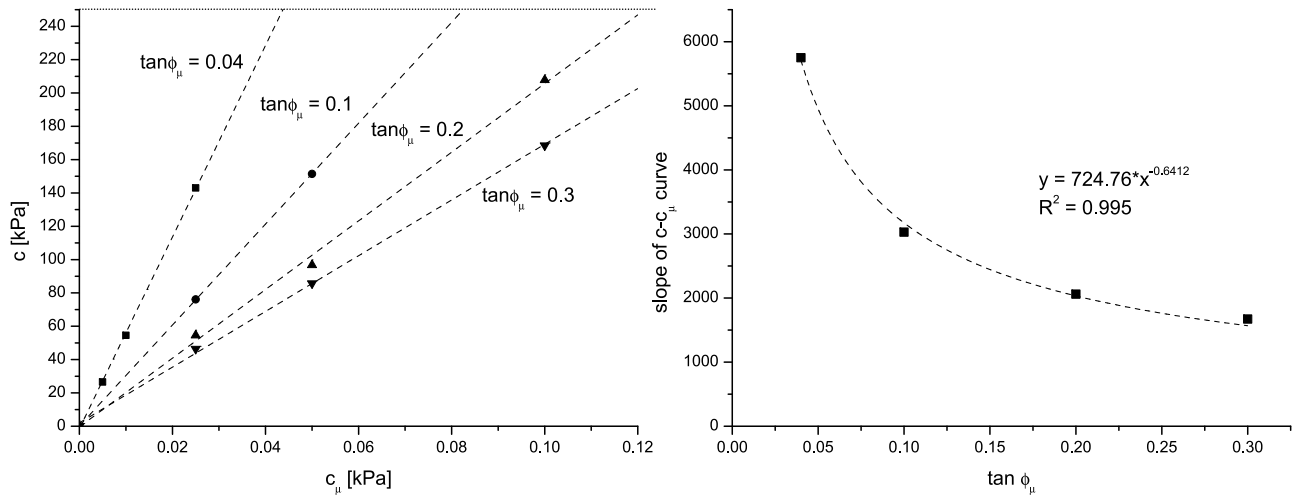
Figure 3. (left) Macroscopic versus microscopic cohesion for various values of ϕ_μ; (right) slope of the $c - c_\mu$ curve versus tan ϕ_μ [after *Utili and Nova*, 2008].

verified by comparison with a few simulations without damping that such a small value does not significantly affect the achieved results in terms of successive cliff front geometries. Finally, this small damping could be thought as an implicit way of taking into account the energy dissipations occurring after a failure takes place because of the inelastic collisions among particles during the propagation phase of the landslides [*Calvetti et al.*, 2000]. In the following, first the case of uniform weathering will be illustrated and then different hypotheses on nonuniform weathering will be introduced.

2.1. DEM Versus LA: Uniform Weathering

[12] A vertical uniform slope 40 m high, with unit weight $\gamma = 20$ kN/m^3 was analyzed. A quite typical value of friction angle ($\phi = 34°$) for natural materials was adopted. After some trials, a suitable geometric domain (see Figure 4) was determined. A large length (3H) behind the cliff front was chosen in order to follow the progressive retreat of the slope. Concerning grain size distribution, it was not possible to assume the particle sizes adopted in the biaxial tests, since the number of elements required to simulate the problem would overcome the capabilities of available computers. Hence, particle sizes were suitably upscaled retaining the same uniform distribution adopted in the biaxial tests. The particle radii were multiplied by a common factor $\rho = 66.7$ in a first simulation case, and $\rho = 200$ in a second simulation case, the total number of particles being 74,405 in the first case and 21,385 in the second case. After the completion of the generation procedure of particles, gravity was applied. Once the system reached static equilibrium, bonds were assigned to contacts. Then, an initial high value of cohesion, around 10 times the value recorded at the occurrence of the first failure determined by the LA method was assigned to contacts. A uniform cohesion decrease was given throughout the slope with the friction angle kept constant. This was implemented by reducing the parameter c_μ stepwise as shown in Figure 5. After each cohesion decrement the assembly of bonded particles reached a new equilibrium configuration.

[13] The field of velocities of the particles recorded just before the occurrence of the first failure is shown in Figure 6a. From Figure 6a, a log spiral contour line delimiting the soil region involved in the failure mechanism can be recognized. This line is very similar to the logarithmic spiral assumed as failure line in the LA approach [see *Utili and Crosta*, 2011], and it passes through the slope toe as in the LA solution (see Figure 6b).

[14] The condition of strong erosion (weathering-limited) was simulated by deleting all the particles detached from the slope before they impacted against the base of the cliff. Figure 6c shows the field of velocities recorded just before the occurrence of the second failure. The shape of the sliding mass is well fitted by a logarithmic spiral and therefore resembles the failure line predicted by LA (see Figure 6d) and finite element analyses with $\phi = \Psi$ [see *Zheng et al.*, 2005]. The successive failures are characterized by mechanisms which involve only a part (the upper one) of the slope front (see Figure 6e), again showing failure lines similar to the ones assumed in LA (see Figure 6f).

[15] In Figure 7 the evolution of the studied slope in terms of normalized cohesion is shown. Concerning the values of cohesion predicted by the DEM for the first failure, if the upscaling factor ρ is reduced, the numerical solution comes closer to the LA solution as can be observed in Figure 7. However, the numerical solution does not seem to converge to the value given by LA but to a lower one, being c/γH still
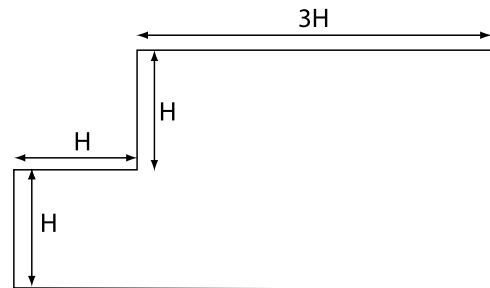

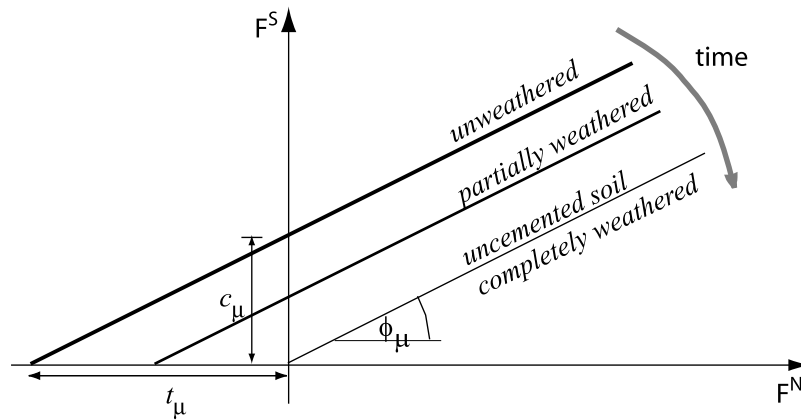**Figure 4.** Domain adopted into the numerical simulations.

Figure 5. Effect of weathering on bonds strength. F^N and F^S are the normal and tangential forces, respectively, acting on the bond.

20% lower than the LA solution for $\rho = 66.7$ which is the lowest value employed for the upscaling factor. In this respect, convergence of the DEM analyses to the LA solution should not be expected for three reasons: (1) LA assumes a dilation angle equal to the friction angle (validity of normality rule), whereas this is not the case for the synthetic material formed by the bonded disks which exhibit a dilation angle ranging from 13.5° to 19.5° ($\phi = 34°$), depending on the value of confining pressure and c_μ; (2) LA does not take into account the effect of progressive failure, whereas a failure develops progressively in the DEM simulations; and (3) the DEM analyses are two-dimensional analyses which differ from a plane strain case since the condition $\varepsilon_z = 0$ (being z the out-of-plane direction) is never enforced throughout the simulations.

[16] Concerning the first point, there is a theorem of LA [*Radenkovic*, 1961] which states that the upper bound limit load in case of a nonassociative material is lower than the upper bound limit load determined assuming associativeness. This implies that the value of the obtained normalized cohesion, $c/\gamma H$, should be higher in case of the DEM simulations ($\psi \neq \phi$) than in case of LA ($\psi = \phi$). Concerning the second point, the question could be formulated in the following way: assuming the slope is made by a geomaterial with associated behavior, if progressive failure is taken into account in the analysis, what is the effect on the predicted collapse load? If progressive failure is taken into account, the resistance of the material along the failure surface is no longer constant but it depends on the accumulated irrecoverable (plastic) strains. As reported by *Nova* [2008], from a theoretical point of view it can be shown that if the limit load is calculated for the case of a slope made of an ideal geomaterial with infinite ductility, that is, constant peak strength, as assumed by LA, and for the case of a real geomaterial with a finite amount of ductility, that is, strength decreasing from the peak value after a certain amount of plastic strains has been accrued, with the same peak strength, the collapse load obtained for the slope is always lower in case of the real geomaterial with limited ductility. In order to investigate the effect of progressive failure, *Potts et al.* [1997] ran FE analyses for c, ϕ slopes, with c, ϕ linearly varying from a peak value till a residual value showing that the obtained rupture surfaces were made by

three parts: near the bottom of the slope, the values of c, ϕ were equal to the residual strength values; near the top they were equal to the peak; and along the central part they varied between peak and residual values. Therefore, Potts et al. introduced the concept of operational strength which is given by values of c, ϕ relative to an equivalent infinitely ductile material. These c_{op}, ϕ_{op} are lower than ϕ_{peak} and c_{peak} and higher than ϕ_{res} and c_{res}. This is another way of saying that if progressive failure is taken into account, the slope turns out to be less stable. However, these analyses may suffer from mesh dependency. In order to avoid the effect of mesh dependency, a nonlocal constitutive relationship should be used in the FE analyses [see *Troncone*, 2005]. In the DEM analyses the effect of mesh dependency is not present and the effect of progressive failure is taken into account since the employed bonds have limited ductility because they break after a certain amount of irrecoverable tangential displacements at particle contacts has been reached. However, no calibration of the ductility of the bonds was carried out in our simulations and the upscaling of particles is likely to affect the results obtained since the particle size employed is bigger than the expected width of a typical shear band in a geomaterial. In conclusion, an analysis taking into account the effect of progressive failure gives rise to a lower value for the collapse load and therefore this effect is analogous to point 1. However, the DEM analyses consider both progressive failure and nonassociativeness of the geomaterial at the same time. Now, it cannot be proved, but it is intuitive to guess that if the two things are combined, a lower collapse load is still obtained. Therefore, according to what has been said so far, the value of normalized cohesion obtained by the DEM analyses should be higher than the values obtained by LA. But this is not the case since the $c/\gamma H$ values predicted by the DEM were lower than the ones predicted by LA (see Figure 7). Therefore, this must be entirely ascribed to point 3. This is confirmed by recent 3-D DEM analyses of the same vertical slope in plane strain conditions [*Gough*, 2010]. In these analyses, an extension of the employed bond model to the 3-D case was used, with ϕ_μ and c_μ calibrated by numerical triaxial tests. Two frictionless walls were used to contain bonded spheres in the out-of-plane direction. All the values of $c/\gamma H$ at the occurrence of the first failure obtained for
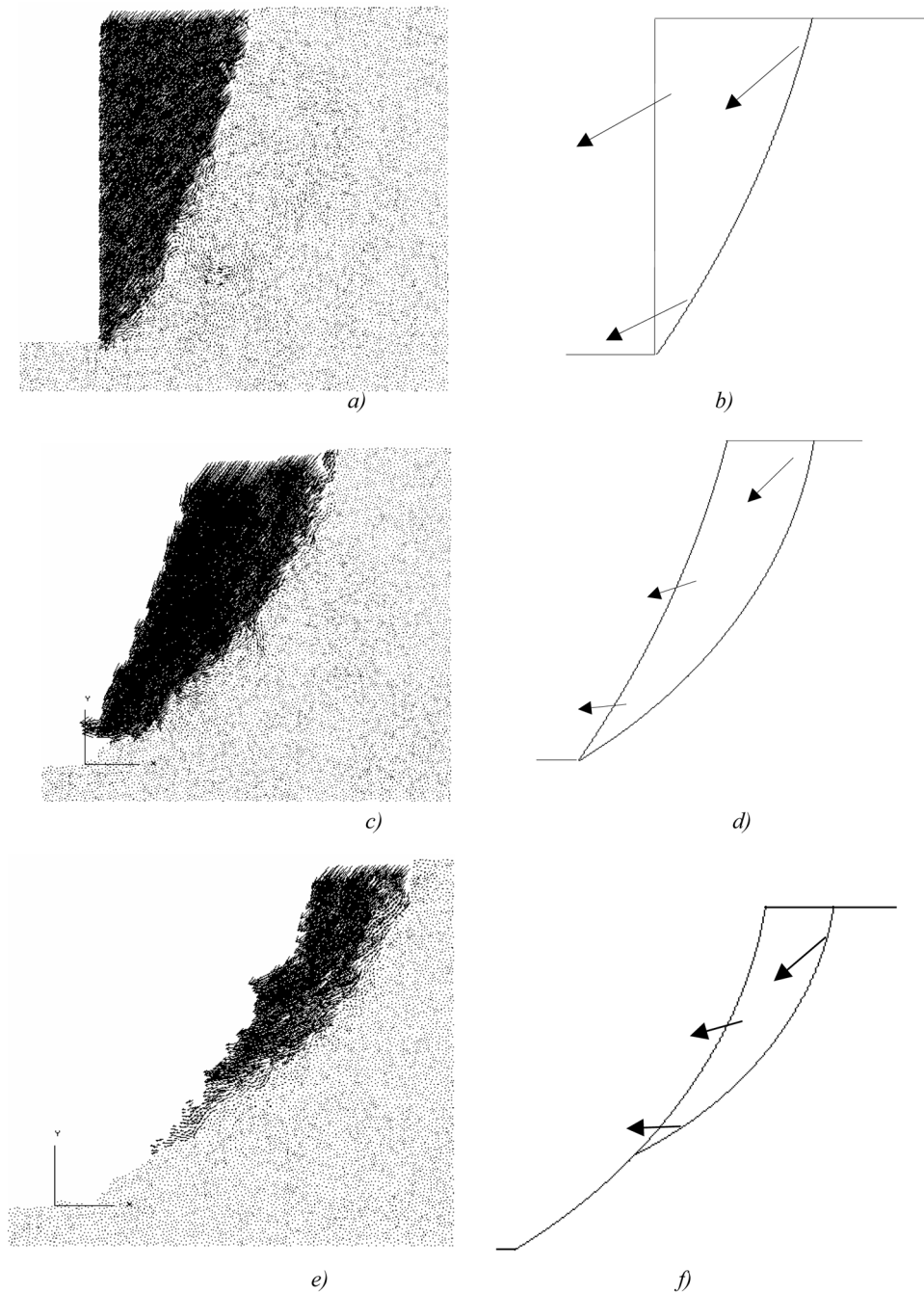
Figure 6. Fields of velocities (the scale is the same for all plots) for an initially vertical slope ($\phi = 34°$) subject to uniform weathering: (a) just before the occurrence of the first failure by DEM, (b) at the onset of the second failure according to limit analysis, (c) at the onset of the second failure by DEM, (d) at the onset of the second failure according to limit analysis, (e) at the onset of the third failure according to the DEM, and (f) at the onset of the third failure according to limit analysis [after *Utili and Nova*, 2008].

various upscaling factors were higher than the value predicted by LA (see Figure 8) in agreement with what should be expected (see points 1 and 2 of the discussion). Moreover, convergence for an increasing value of the upscaling factor (ρ) to a higher value than the one predicted by LA is observed. In case of 2-D DEM analyses instead, convergence of the numerical solution toward a value lower than the LA solution is observed (see Figure 8). This means that

the lack of imposition of the plane strain condition ($\varepsilon_z = 0$) leads to an overestimation of the collapse load.

2.2. Nonuniform Weathering

[17] After the model validation it is now possible to simulate more realistic weathering scenarios. In fact, weathering is due to an ensemble of chemical and physical actions on both hard soils and weak/hard rocks which is
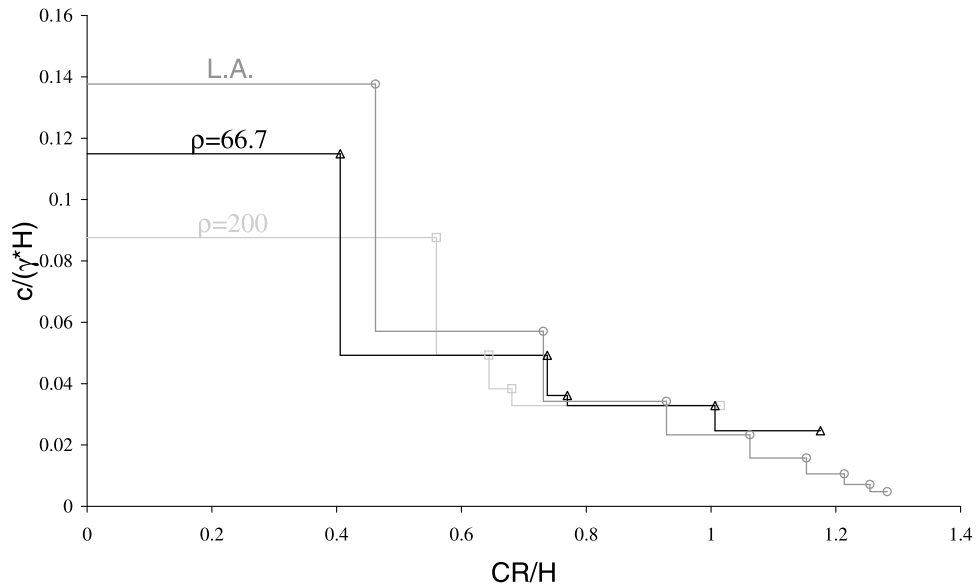
Figure 7. Dimensionless crest retreat versus normalized cohesion for an initially vertical slope ($\phi = 34°$) subject to uniform weathering by DEM analyses [after *Utili and Nova*, 2008].

certainly nonuniform in space and changes over time. *Utili and Nova* [2008] presented the case of an initially vertical cliff subject to weathering propagating along two fronts: the exposed cliff forefront, and a horizontal front from the cliff top both moving inward at constant velocity. In that paper, it is also shown that there are two types of landslide mechanisms called "wedge" and "scratch." The former one consists of a deep mechanism caused by the detachment of a log spiral block whereas the second one consists of the progressive detachment of soil particles lying along the cliff forefront. The

occurrence of one of the two types of failure depends on the thickness of the weathered layer of material within the cliff.

[18] Here the numerical model will be applied in comparison with predictions obtained by the well established, Fisher-Lehmann [*Fisher*, 1866; *Lehmann*, 1933] and Bakker–Le Heux [*Bakker and Le Heux*, 1946, 1952] geomorphologic models. Weathering will be considered acting only along one front of propagation, initially parallel to the exposed cliff surface. By means of the established calibration procedure, it is possible in principle to model any type of degradation of both cohesion and friction according to some
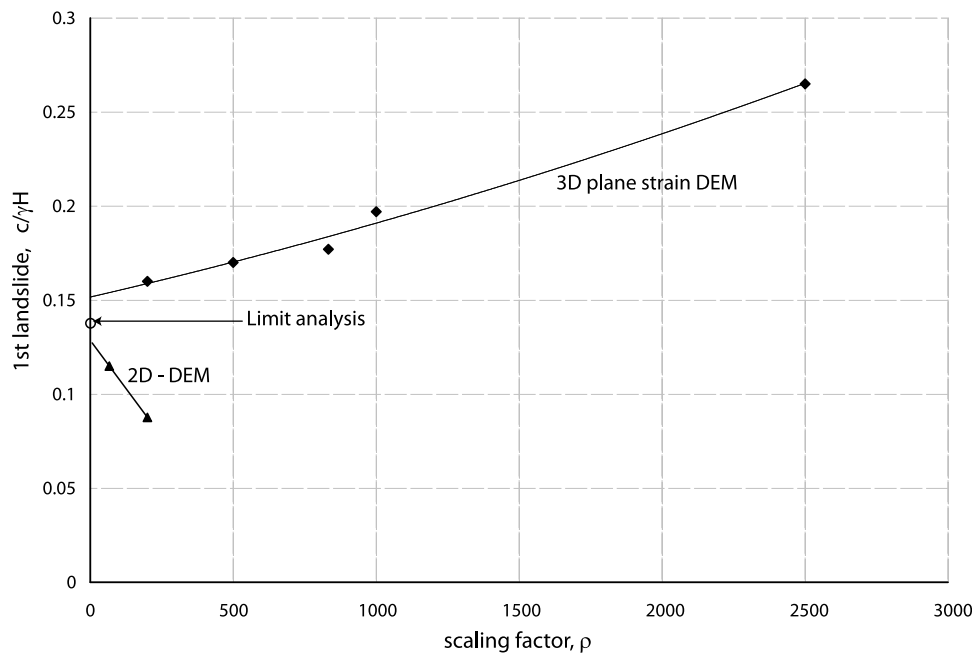

Figure 8. Values of $c/\gamma H$ at the occurrence of the first failure for an initially vertical slope ($\phi = 34°$) subject to uniform weathering for different values of the scaling parameter ρ, in cases of 2-D and 3-D plane strain analyses by the DEM.
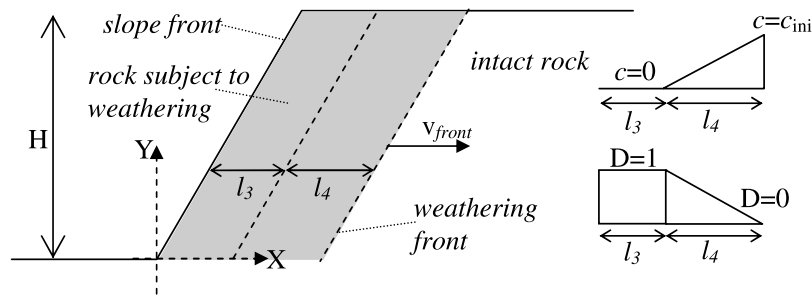
Figure 9. Weathering within the slope as time elapses. The reference axes are indicated by dashed lines.

known laws $\phi = \phi(t)$ and $c = c(t)$, since there is a biunivocal correspondence between any c, ϕ pair of values and the corresponding c_μ, ϕ_μ pair of micromechanical parameters (see equations (1a) and (1b)). However, the available experimental data about the variation of material strength within natural slopes are scanty, and therefore it was decided to reduce only cohesion to keep things simple and make it easier to draw comparisons with other geomorphologic models.

2.2.1. Case of Parallel Weathering Propagation

[19] In the first case, weathering is assumed to propagate along a front parallel to the exposed cliff inward (i.e., slope retreat at constant angle) [*Schumm*, 1956]:

$$X_{front}(t) = 0 + v_{front} \times t, \tag{3}$$

where X_{front} is the X coordinate and v_{front} is the velocity of the weathering front (i.e., weathered thickness per unit time) which was assumed to be parallel to the initial cliff forefront (see Figure 9). The degradation of the cliff region subject to weathering (gray zone in Figure 9) was assumed to be

$$D(t) = (X_{front}(t) - X)/l_4 \text{ with } 0 < D < 1, \tag{4}$$

where D is the damage index for the generic contact bond located at (X, Y), while l_4 represents the distance over which damage linearly varies from 0 to 1. Considering a generic instant of time t, damage will be zero within the inner intact zone of the slope, then it will linearly vary from 0 up to 1 and it will be uniformly 1 in the zone, l_4 wide, of fully weathered material (see Figure 9). The variation of cohesion over time is given by

$$c(t) = c_{ini}(1 - D(t)). \tag{5}$$

Since the spatial distribution of weathering changes over time, it is necessary to explicitly assume an initial condition to simulate the progression of degradation with time unlike the case of uniform degradation. The initial condition assumed at t_0, was that of unweathered material: D = 0 throughout the whole slope. This assumption supposes the existence of a time when the cliff was characterized by a uniform strength which could be thought as the time of formation of the cliff: for instance, the formation of a scarp or a hillslope because of a deep-seated landslide [see *Utili and Crosta*, 2011, section 3.4], a series of rapid displacements along a specific plane (e.g., fault) or erosion and deposition of river terraces. This is also the standard assumption in the Fisher-Lehmann and Bakker–Le Heux

models. A constant rate of degradation v_D was assumed in all the points subject to weathering. This parameter represents the damage rate: that is the increment of D over time. Therefore the distance l_4 in equation (4) was determined accordingly:

$$l_4 = v_{front} \times \frac{1}{v_D}. \tag{6}$$

[20] Depending on the value of l_4, two different failure mechanisms may take place. If the transition between the intact and the fully damaged zone is sharp (low l_4 values), particles detach gradually and progressively following the penetration of the degradation front from the cliff forefront. On the contrary, when the transition is smooth, that is, there is a large distance between the intact and the fully damaged zone (high l_4 values), the movement of a large part of the cliff occurs. The two mechanisms could be referred to as scratching/raveling and block failure. The block failure types have already been reported by *Utili and Crosta* [2011].

[21] In the case of a raveling failure, once particles start falling off, they progressively accumulate at the base of the slope and the process of detachment continues until all the debonded particles at the top of the cliff get sustained by the debris accumulated at the cliff toe. This situation corresponds to transport limited erosion. In this case, single or small groups of particles detach from the cliff as weathering moves forward, therefore it is not possible to identify discrete events of failure and the crest retreat can be considered continuous over time. In this case, the crest retreat rate is governed by the rate of penetration of the weathering front.

[22] The rate of weathering is usually quite slow: from some decades to several centuries depending on the type of material and the environmental conditions. Therefore, the rate of weathering needs to be scaled to a much higher value to run simulations in a feasible computational time. To do so, we wanted to assign the highest possible v_{front}^{sim} (velocity of propagation of the weathering front in the simulations). At first, it could be thought that any v_{front}^{sim} is acceptable since a cliff subject to weathering remains under quasi-static conditions. However, if the adopted v_{front}^{sim} is too high the bonds do not have time to break off and then soil failure is detected with a delay. This leads to an overestimation of the times of failure leading, in turn, to an overestimation of the cliff stability. In conclusion, weathering is induced so quickly that the increment of weathering per computed time step is too large to correctly simulate the process. To choose a
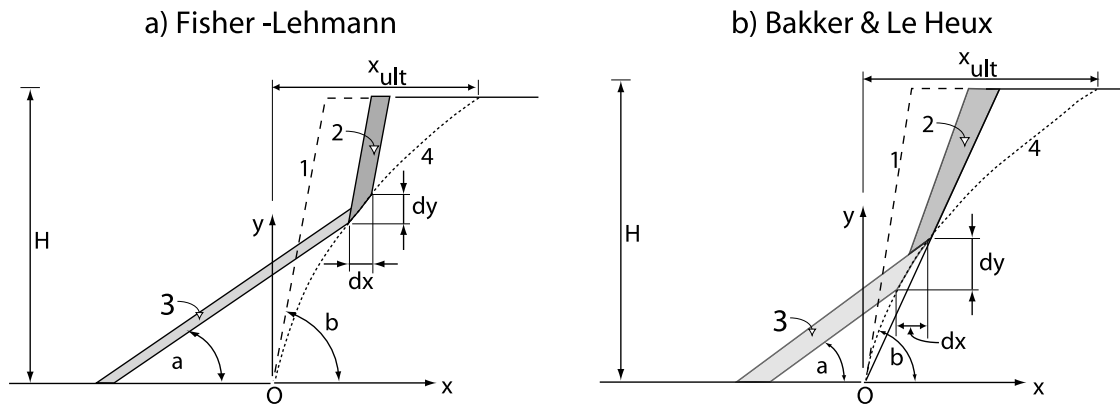
Figure 10. (a) Parallel crest retreat (Fisher-Lehmann model) [*Fisher*, 1866; *Lehmann*, 1933]. (b) Inclined crest retreat (Bakker–Le Heux model) [*Bakker and Le Heux*, 1946, 1952]. Drawings after [*Hutchinson and Stuart*, 2003].

proper v_{front}^{sim}, some sensitivity analyses were performed. Having taken $l_4 = 2$ m, $v_{front}^{sim} = 3.17$ m/s proved to be the highest possible velocity without getting an undue delay of bond breakages and debris transport onset with respect to the advancement of the weathering front. Now, it has to be noted that according to our assumptions, once l_4 is prescribed, v_{front} and v_D are related by equation (6). Therefore only one of them can be independently chosen with the other parameter determined by equation (6). Given a certain type of geomaterial, v_D is a property that can be experimentally determined, then v_{front}^{real} is constrained trough equation (6) by having assumed $l_4 = 2$ m. Then, the ratio, C, between the real time and the simulation time is given by

$$C = \frac{v_{front}^{sim}}{v_{front}^{real}}. \tag{7}$$

This upscaling time factor will be further discussed in section 3.

[23] In order to identify the onset of a failure the kinetic energy of the system and the number of breaking bonds were monitored as in the case of uniform weathering. When dynamic forces within the system became significant, weathering was stopped and the elapsed time was recorded. Then cycles were run to follow the evolution of the moving particles until the system reached again a condition of static equilibrium. At this point, weathering was resumed and the process of degradation continued until the subsequent soil movement took place.

2.2.2. Comparison With Other Cliff Retreat Models

[24] Of the many cliff retreat/degradation models proposed in the literature [*Fisher*, 1866; *Lehmann*, 1933, *Bakker and Le Heux*, 1946, 1952; *Scheidegger*, 1961; *Carson and Kirkby*, 1972; *Young*, 1972; *Andrews and Hanks*, 1985; *Obanawa and Matsukura*, 2006], the earliest ones [*Fisher*, 1866; *Lehmann*, 1933, *Bakker and Le Heux*, 1946, 1952] are considered the most relevant for our problem and therefore will be used to be compared with the results obtained by DEM analyses hereafter. These models have been applied to different geological and geomorphological conditions and also on relatively well constrained in situ experiments [*Jewell*, 1963; *Bell et al.*, 1996; *Hutchinson*, 1998]. The main assumptions of the Fisher-Lehmann model are (see Figure 10a): (1) an initially straight slope of uniform material of inclination β, steep enough for debris removal not to be transport limited; (2) a slope with horizontal ground at its foot and crest; (3) no water is present; (4) in a given time, weathering produces an equal retreat of all parts of the exposed free face by the falling away of fine debris without consideration for major block type mechanisms; (5) a convex outward shape is produced in the surface of the intact rock beneath the scree; (6) in the limit the original cliff develops into a straight slope inclined at the scree angle to which, in its last formed upper part, the underlying convex core rock is tangential; and (7) the resulting debris accumulates contemporaneously at the cliff foot as a rectilinear scree of constant angle $\zeta < \beta$.

[25] All simulations have been run retaining assumptions 1, 2, and 3, that is, to consider an initially dry inclined slope as shown in Figure 9. By means of numerical analyses it is now possible to run simulations to check which assumptions among 4, 5, 6, and 7 are true and which are false. The comparison between our numerical results and the geomorphologic models is made in terms of geometry for both cliff and talus; therefore, the total time of degradation is of no interest. Depending on the velocity of the degradation front v_{front} and the damage rate v_D, the predicted slope evolution could take place in years, decades or centuries.

[26] In the Fisher-Lehmann model it is assumed that beneath the accumulating scree, the intact rock surface is protected from further weathering, while the exposed rock face above continues to weather and retreat. Then, in this first set of simulations, no reduction of weathering was assumed due to the presence of the scree. In fact, it is very difficult to quantify the protection given by the scree in terms of weathering which depends on the porosity and particle size distribution of the debris material. Moreover, from a computational point of view, it is extremely difficult to make weathering intensity dependent on the accumulated scree since the scree material does not lie along a straight line and changes every time particles fall from the exposed cliff face. However, in the following, a different type of weathering propagation will be considered (see section 2.2.3) which takes the protective effect, due to the presence of
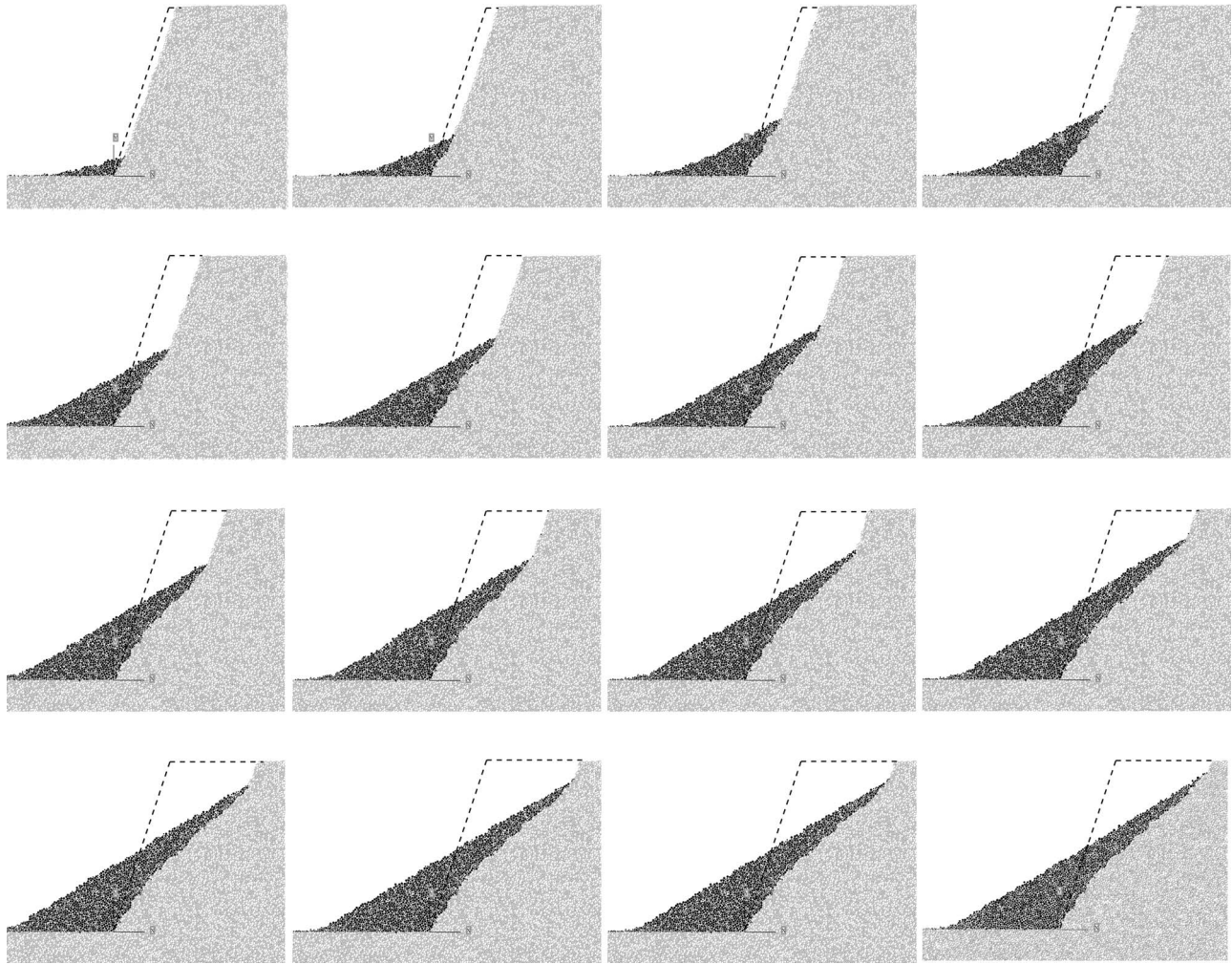
Figure 11. Evolution of a cliff initially inclined 70° on the horizontal, $\beta = 70°$, subject to parallel weathering propagation. Particles which displaced more than 2 m are black, whereas particles which displaced less than 2 m are white and gray-contoured. The dashed line represents the initial cliff.

the scree, implicitly into account. On the other hand, the stabilizing effect of the scree weight over the cliff toe is fully taken into account in all the DEM analyses.

[27] In Figure 11, the sequence of cliff profiles obtained having assumed a parallel weathering front with $l_4 = 2$ m is shown. Particles are shown with two different colors: dark particles are debris material forming the scree, whereas light colored particles belong to the original cliff. All these snapshots have been taken in static situations, after falling particles stopped running (i.e., negligible kinetic energy of the system $E_{kin} \approx 0$). Looking at the sequence of images it is possible to see that the cliff underwent a parallel retreat since the free cliff front remains parallel to the dashed line corresponding to the initial cliff front. This leads to conclude that assumption 4 of the model is true: that is, when major block type mechanisms do not occur, weathering produces an equal retreat of all parts of the exposed free face which in fact keeps the same inclination during the entire retreat process (see Figure 11).

[28] Assumption 5 concerns the presence of an intact core of material which does not displace during the entire cliff degradation process. In order to identify this core, in all the

images of the degrading cliff two colors have been used. As it can be seen in Figure 11, the shape of this core evolves during the various stages of degradation until it reaches a form which is similar in shape to the Fisher-Lehmann core, more qualitatively rather than quantitatively. To calculate the shape of the curve of the nondisplaced material predicted by the Fisher-Lehmann model, the following equation has been used:

$$X = k(l + m) \ln[m/(m - Y)] - kY, \qquad (8)$$

where $m = h/d$, $k = (a - ad - b)$, $l = bh/(a - ad - b)$, $a = \cot\zeta$, $b = \cot\beta$, $d = 1 - 1/\text{bulking factor} = 1 - \text{volume of intact soil/volume of debris}$; X, Y, h, α and β are as defined in Figure 10a. The variable ζ has been given the value of the final scree inclination, 31°, whereas β is equal to the initial cliff slope, 70°. Then, to obtain d, it is necessary to calculate the ratio of the area of intact soil fell off the cliff and the area of debris accumulated at the cliff toe. The obtained value, d = 0.058, is very low compared to values reported in the literature. This is due to the two-dimensional (2-D) nature of our analysis. In fact, the porosity of an assembly of 2-D
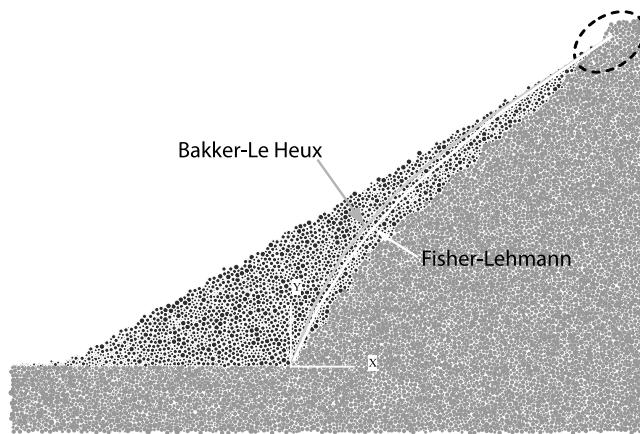
Figure 12. Case of parallel weathering front. The gray particles show the core obtained by the DEM analysis; the white and gray lines indicate the shape of the core predicted by the Fisher-Lehmann and the Bakker–Le Heux models, respectively.

disks is significantly lower than the porosity of 3-D spheres and real material particles (in our case the initial disk porosity is $n = 0.16$). As a consequence, also the bulking factor, given by the ratio between the area occupied by the initially bonded disks and the area occupied by the debonded disks, forming the final debris, cannot reflect the real ratio present in nature. This ratio could only be obtained if a 3-D analysis would be run. However, this limitation does not prevent a meaningful comparison with Fisher's model since the low bulking ratio obtained from our numerical simulations, $d = 0.058$, has been used in equation (8) to draw the curve of the Fisher's model shown in Figure 12. For sake of completeness, also the shape obtained from the Bakker–Le Heux model has been included in Figure 12 (see equation (9)).

[29] Considering now assumption 6, this holds true. In fact, the final scree inclination is tangent to the underlying core of nondisplaced material. In the uppermost part of the cliff (see the region enclosed by a dashed circle in Figure 12), it may be noted that the inclination of the final scree seems to diverge from the tangent to the Fisher's line of undisplaced material. In reality this may be ascribed to the size effect of the particles used. In fact, if smaller particles were used this effect would not be apparent. All the bonds among these particles were broken, but the particles did not move from their location downward because of local geometrical effects due to the fact that the number of particles in such a small region becomes too small.

[30] Concerning assumption 7, the numerical analyses indicate that this assumption does not hold true. Looking at the scree it can be noted that the talus profiles are, albeit slightly, concave and their average gradient is least and their concavity greatest when the scree is low relative to the cliff height. These results are also in agreement with evidence from experimental talus slopes and results from *Kirkby and Statham* [1975] and *Kirkby* [1987]. According to our analyses, the concave shape may be attributed to dynamic

effects. In fact, similar concave shapes have been obtained both numerically and experimentally from the collapse of 2-D granular material columns initially vertical on a rough horizontal bed from *Lube et al.* [2004], *Lacaze et al.* [2008], and *Crosta et al.* [2009]. Furthermore, the talus shape becomes less and less concave as the crest retreat progresses until eventually it becomes straight. The progressively decreasing concavity may be explained thinking of the kinetic energy of the particles detaching from the cliff surface. The higher this energy is, the farther away the particles move after their impact with the accumulated talus. Therefore, as the talus becomes higher, the distance run by each particle from the point of detachment to the point of impact with the existing talus decreases, and with it the kinetic energy available to the particles as well. So the particles in the end tend to accumulate along a straight line whose inclination is near the angle of repose of the debonded material. In this case the final inclination of the talus is about 31° over the horizontal. The variation of average talus slope with talus height is summarized in Figure 13 where a linear trend in a semilogarithmic graph is shown. This trend is in agreement with what reported by *Kirkby* [1987]. Thus, if one wants to neglect the effect of the dynamic fall of particles, assumption 7 may be retained. Indeed, there may be other factors affecting the scree concavity such as basal removal, wind erosion, slope wash, etc., but both our model and Fisher–Lehmann model do not intend to address them.

2.2.3. Inclined weathering propagation

[31] In the Bakker–Le Heux model, the same hypotheses as in Fisher-Lehmann's are taken with the exception of the inclination of the advancing weathering front (assumption 4), controlled by a rate of weathering linearly increasing with elevation starting from the initial slope toe (see Figure 10b). This can also be expressed as a change of the inclination of the free cliff face (i.e., declining angle of retreat) [*Schumm*, 1956] obtained as a progressive rotation about the initial cliff toe (point O) as shown in Figure 14. In our analyses, weathering has been assumed accordingly, with a propagation front that no longer propagates horizontally but whose inclination rotates around the initial cliff toe as shown in Figure 14. The velocity of weathering propagation, v_{front}, now depends on the elevation of the point of the front considered, but is constant with time along any horizontal line. This type of weathering occurs when the exposure to atmospheric agents is larger in the upper part of the slope than in the lower one. Furthermore, such a weathering distribution can also be thought as taking into account the protection against weathering exerted by the talus covering the lower part of the cliff.

[32] In Figure 15 some sequences of the cliff retreat process are shown. Again, dark particles represent the debris material forming the scree, and light-colored particles the material which did not displace. The sequence of images shows that the cliff underwent a retreat which is no longer parallel but with decreasing inclination to the horizontal. In fact, the inclination of the free cliff front remains parallel to the rotating weathering propagation front. This leads to conclude that assumption 4 of the model is true: that is, when major block type mechanisms do not occur, weathering produces a cliff retreat characterized by the rotation of the free face around the initial toe of the cliff.
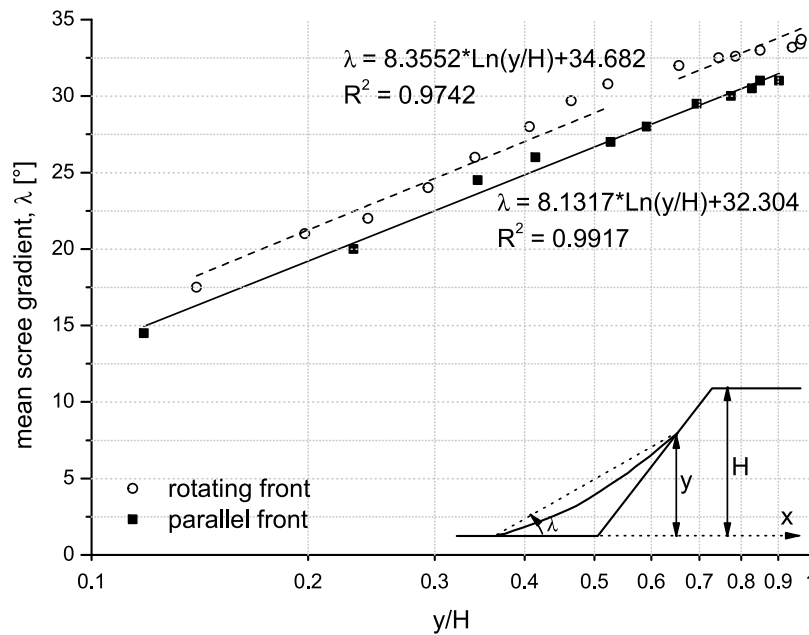
Figure 13. Mean talus inclination versus talus height at various stages of slope degradation. Note that the scale is semilogarithmic.

[33] Looking at the shape of the core of nondisplaced material, the Bakker–Le Heux model predicts a different shape according to the following equation:

$$X = aY - (a - b)Y\left[\left(h^2 + (1 - 2d)Y^2\right)/h^2\right]^{\frac{(d-1)}{(1-2d)}}, \quad (9)$$

with symbols as defined in equation (8). In Figure 16, the shape of the core of nondisplaced material obtained by the numerical analysis can be compared with the Bakker–Le Heux model predictions. In this case, the two shapes are in a significantly better agreement. For sake of completeness, the shape obtained from Fisher-Lehmann model has also been included in Figure 16. In this case the final inclination of the talus is about 33.5° over the horizontal. Finally, it can be noted that also the final scree linear inclination is tangent to the upper part of the curve marking the border with the intact core material as predicted by the Bakker–Le Heux model.

[34] Depending on the type of weathering penetration, the kinematic mechanisms leading to soil failure are different as it can be seen in Figure 17. In the case of a parallel advancing weathering front, a flow of particles along a line parallel to the front takes place. The velocity of particles moving out of the column is roughly uniform as it can be noted from the length of the plotted velocity vectors which is proportional to their magnitude. On the contrary, in case of rotating weathering front, it is evident that particles start falling from the top of the slope and they push down the particles lying below.

3. Transport Law

[35] As above described, slope material is transported downslope after each successive failure episode. In general, the initial failures are followed by longer transport lengths because of the higher fall height experienced by the detaching particles before hitting the talus slope. Successive failures are characterized by smaller volumes and fall heights. The adopted DEM approach allows the computation of the volume and mass of material passing through the slope toe
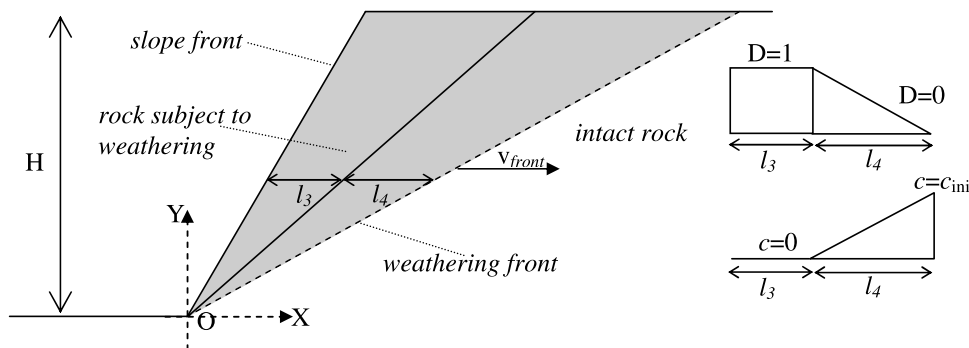

Figure 14. Weathering with inclined propagation front rotating around the cliff toe, O. The velocity v_x is constant over time.
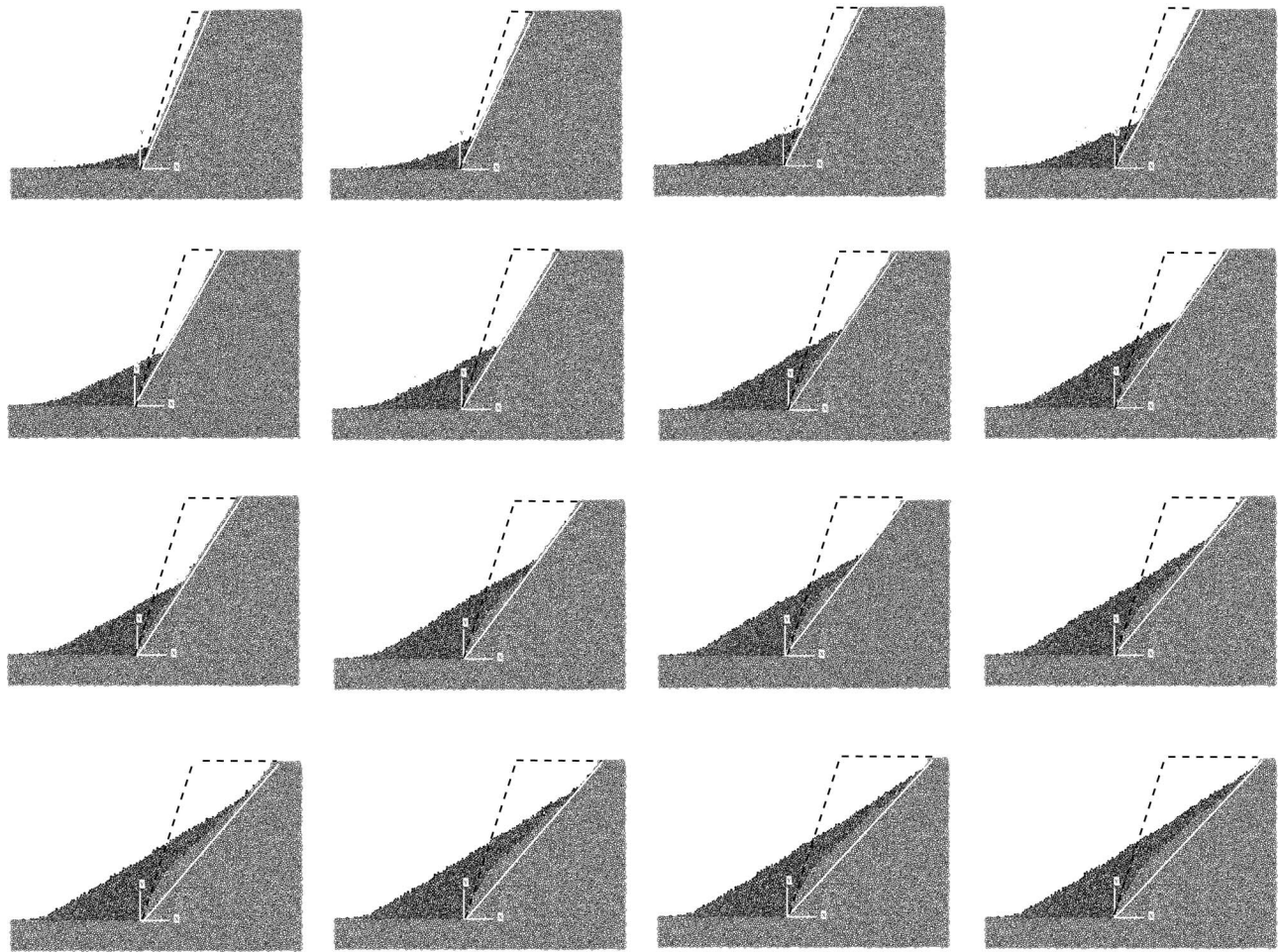
Figure 15. Evolution of a cliff initially inclined 70° ($\beta = 70°$), subject to rotating weathering penetration. Particles which displaced more than 2 m are black, whereas particles which displaced less are white and black-contoured. The solid white lines represent the evolving weathering front while the dashed black lines represent the initial cliff profile.

at different times. Nevertheless, a congruous time interval is required to obtain results independent of the adopted particle size and therefore of the particle radius upscale coefficient, ρ. In fact, the rate of mass transport is affected by the size of the adopted particles. Because of computational time requirements, particles have been upscaled; therefore a longer time interval is required for a layer of one particle in thickness to fail in the numerical simulations than in reality. If particle size is decreased keeping the same degradation rate, the mass flux starts earlier in comparison with the case of a larger upscale coefficient.

[36] The evolution of the slope in terms of geometry of the generated talus is represented in Figure 13 both for the case of a parallel and a rotating weathering front advance. In both the cases, the mean scree slope gradient increases rapidly during the initial failures (i.e., low y/H ratio) to reach the internal friction angle value only after a large number of successive failures. At the final step, when the y/H ratio tends to 1, the scree slopes are at about the angle of repose. This phenomenon has been observed and modeled in granular step collapse experiments [*Lajeunesse et al.*, 2004; *Lube et al.*, 2004, 2005; *Siavoshi and Kudrolli*, 2005;
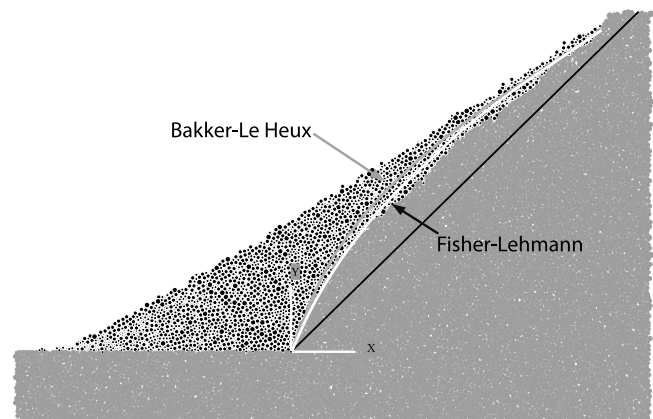

Figure 16. Case of rotating weathering front. The gray particles show the core obtained by the DEM analysis; the white and gray lines indicate the shape of the core predicted by the Fisher-Lehmann and the Bakker–Le Heux models, respectively.
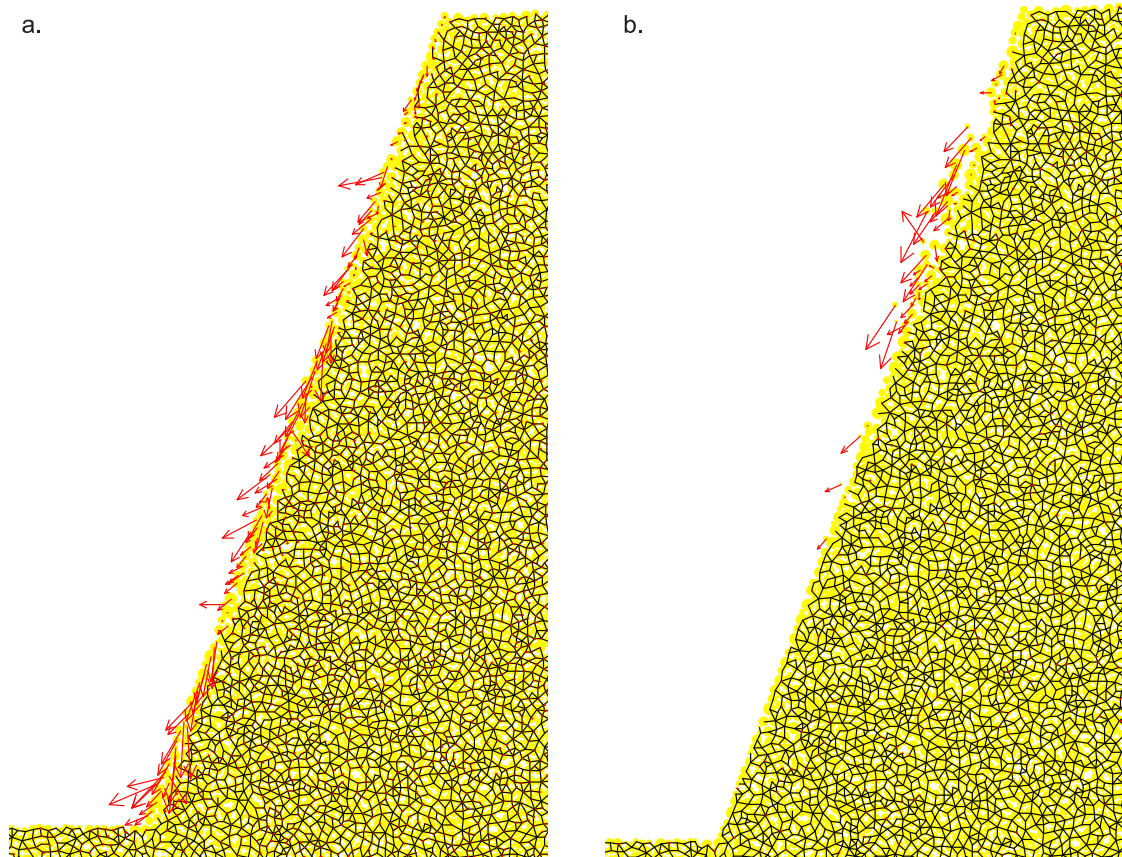
Figure 17. Kinematics of the failure mechanisms taking place. The red arrows represent particle velocities, and the black lines represent the intact bonds; disks are yellow-colored. (a) Case of parallel advancing weathering front; (b) case of rotating weathering front.

Balmforth and Kerswell, 2005; *Crosta et al.*, 2009]. Eventually, the talus evolves from a concave upward profile to a progressively more linear geometry, with a slow advance of the extreme scree toe (defined by excluding the most extreme particles; see, for example, Figure 12). This result agrees from a qualitative viewpoint at least, with observations made directly in the field [see *Kirkby*, 1987].

[37] If an accurate quantitative investigation of the talus base evolution and debris runout distances are sought, a more refined modeling of the contact laws would be needed. For instance, *Taboada et al.* [2006] proposed micromechanical laws including not only frictional sliding, as in this study, but also frictional rolling, by means of a moment-relative rotation relationship at particle contacts and cohesive bonds of a fixed tensile strength gluing two particles over a characteristic finite elliptical length. However, if this approach is followed, an infinite number of combinations of μ_s and μ_r values (i.e., sliding and rolling frictions, respectively) could generate the same macromechanical friction, ϕ [*Estrada et al.*, 2008]. The same can be said for combinations of different tensile strength values and size of elliptical bonding lengths which correspond to the same macromechanical cohesion c. Therefore, the problem lies in the current lack of experimental evidence about geomaterial behavior at the microscale. Because of this, the real micromechanical rolling and friction angles, bonding lengths and tension are unknown, making the choice of μ_s, μ_r pairs, and bonding

lengths and strengths, arbitrary. A lengthy calibration would be required. This choice is likely to affect the behavior of the granular flow and therefore the runout distance of the flow as shown by *Taboada and Estrada* [2009], at least for the case of different μ_s, μ_r values, since energy dissipation partly occurs because of frictional rolling and partly because of frictional sliding. In our model, there are only two micromechanical parameters ruling the contact mechanics between particles making possible a biunivocal correspondence between the known macro mechanical strength parameters (c, ϕ) and the unknown to-be-calibrated micromechanical strength parameters (c_μ, ϕ_μ). The main limitation of the adopted model is that in order to obtain macromechanical friction angles higher than 25°, particle rotation must be inhibited [see *Calvetti and Nova*, 2004] making it impossible to take into account frictional energy dissipation by rolling. This in turn affects the material runout and might affect the talus profile at different times. Nevertheless, the purpose of this paper is not the investigation of runout distances but the evolution of a slope subject to weathering in terms of forefront and talus geometries. The comparison with experimental data from *Kirkby* [1987] shows that the adopted model is refined enough to capture the talus evolution at least from a qualitative point of view. More refined models would require longer computational times not well suited for the simula-
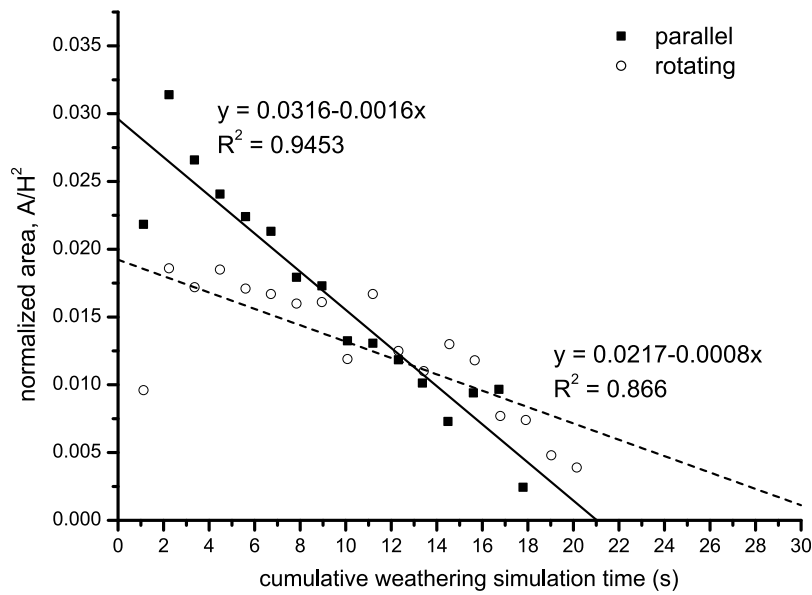
Figure 18. Mass transport in terms of normalized landslid areas versus cumulative weathering simulation time: the transported incremental mass during a time interval is represented by black squares in the case of a parallel propagation front and by gray circles in the case of a rotating front.

tion of slope evolution where many dynamic events (i.e., landslides) take place.

[38] The average mass flux at the slope toe has been computed at different time steps for both cases of advancing degradation fronts. Figure 18 shows that in case of parallel retreat of the slope the mass transport decreases more rapidly than for a rotating front. Times are given in terms of simulation times. Given v_D, the rate of degradation for the geomaterial of interest, the real time can be obtained by using equations (6) and (7). The results show a decreasing linear trend which allows us to estimate the time needed for the slope to reach its final morphology. The case of a rotating front requires more time for the slope to reach its final stage. Having assumed a constant v_D, the results for the case of weathering linearly increasing with time are shown in Figure 18. Furthermore, if larger particles were used, then a slight scattering of the slide areas (and volumes) would occur around a linear trend as shown in Figure 18.

[39] The evolution of the average slope inclination with the size of the failing slices and for different front advances is represented in Figure 19. Here the average slope is computed according to *Utili and Crosta* [2011, equation (8)].
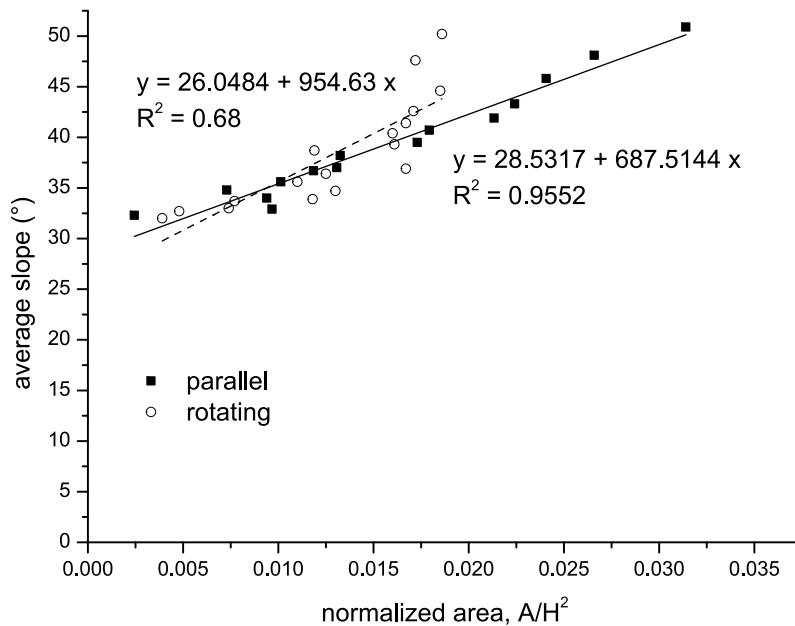

Figure 19. Average slope inclination versus normalized area for the two analyzed cases of weathering propagation, parallel and rotating.

The normalized area values in this plot are larger than those computed for the LA approach. This is an intrinsic problem of the analysis performed through the DEM method, where particles have a finite volume that limits the size of the smaller failures and controls the progressive evolution. The plot shows a linear trend for the case of parallel retreat with failures that are initially much larger, almost twice, than those for the case of a rotating front. In fact, in this last case the initial failures are characterized by similar areas till the 3rd to 4th failure. After these failures occur, the evolution follows the same linear trend observed for the parallel weathering propagation mode. Because of the limitations in the model, related to the chosen particle upscale, we are unable to say if a nonlinear trend can compare for very small failures as observed in the case of the LA approach [see *Utili and Crosta*, 2011, Figure 16].

4. Conclusions

[40] A model based on mechanics to predict the evolution of slopes has been set up. With this model it is possible, to associate quantitatively the evolution of natural slopes to the degradation of strength properties of the geomaterial with time. It has been shown how mechanical parameters and their weakening due to weathering affect the slope profiles. The results of this modeling approach have been compared to those of an analytical model, based on the LA upper bound method, and to other geomorphologically based models.

[41] The appeal of the LA approach in comparison with the numerical method consists in the fact that it provides an analytical solution and results can be presented as tables or nomograms. LA model has some limitations (e.g., homogeneous strength degradation, assumption of associativeness, no consideration for progressive failure), it has been applied only to the case of weathering-limited conditions and it can be applied with some difficulties to more general conditions.

[42] On the contrary, 2-D discrete element method (DEM) analyses were run to numerically model the evolution of slopes subject to both uniform and nonuniform weathering, both for weathering-limited and transport-limited conditions. First, simulations for the case of uniform weathering were run in order to compare the proposed methodology with the results obtained by LA.

[43] In principle any scenario of nonuniform weathering could be modeled by the DEM. It was shown that depending on the extension of the weathered region within the slope, failure can occur involving either an extended mass sliding (block type failure), or a continuous peeling of material off the cliff face, here called scratch failure. So this methodology may be used for both cases of slope evolution characterized either by a discrete succession of mass landslide events or a continuous peeling off the cliff face.

[44] Two established geomorphologic models, namely Fisher-Lehmann [*Fisher*, 1866; *Lehmann*, 1933] and Bakker–Le Heux [*Bakker and Le Heux*, 1946, 1952; *Hutchinson*, 2001; *Hutchinson and Stuart*, 2003], focus on the latter type of slope evolution. In order to assess the assumptions made by these two models, two cases of weathering were considered: one characterized by a front of propagation parallel to the cliff face, and another characterized by a front

rotating about the initial cliff toe. The validity of the assumptions of the two models has been discussed in the light of the results obtained. Concerning the shape of the evolving cliff profile there is a good agreement between numerical simulations and the mentioned models. It was shown that the shape of the scree accumulating at the cliff base becomes linear only at the end of the process, being concave in all the previous stages. This must be ascribed to the kinetic energy of the fallen material which tends to run further away after impacting against the cliff base. Such dynamic effects are not directly taken into account in current geomorphologic models. The presented results have been obtained for the case of blocked particle rotations. If particles were left free to rotate, longer particle runout distances might have been observed.

[45] DEM computational cost is proportional to the number of particles used and the number of dynamic events occurring during the slope evolution. Nevertheless, it has been demonstrated that reasonable results can still be obtained by adopting a reduced number of larger particles, so making simulations feasible.

[46] Three-dimensional plane strain DEM analyses are certainly an area of research to be explored given the predictable increasing availability of computational power and possibly parallel DEM codes., These will allow to investigate how much the results obtained by means of 2-D analyses might be different and the role played by three dimensionality of particles in terms of debris stability and transport. Concerning our future research work, the effects of the introduction of different weathering/alteration and front advancement laws on the geomorphological evolution of slopes (i.e., type of instability and geometry of failures), as well as effects of partial and total deposit erosion from the slope toe will be analyzed through DEM analyses.

Notation

α inclination of the slope summit.
β initial inclination of a straight slope/cliff.
γ unit weight.
γ' submerged unit weight.
$\dot{\gamma}$ angular strain rate.
$\dot{\varepsilon}$ normal strain rate.
ζ scree inclination.
θ, θ^o generic logarithmic spiral angle.
λ inclination of the linear envelope.
ρ particle radii scaling factor for DEM simulations.
σ normal stress.
τ shear stress.
ϕ internal friction angle.
ϕ_μ micromechanical friction angle.
Ψ dilation angle.
$\dot{\omega}$ rotation rate.
a acceleration.
c cohesion.
c_μ micromechanical cohesion.
d bulking ratio.
h height of part of the slope.
k_1, k_2, k_3, k_4 constant coefficients.
l arc length as defined by *Utili and Crosta* [2011, Figure A2].

l_1, l_2 lengths.

l_3, l_4 lengths.

m mass.

n porosity.

r radius of curvature.

r_x^n minimum radius of curvature of the logarithmic spiral of the current failure mechanism.

r_x^o minimum radius of curvature of the old (previous failure) logarithmic spiral.

r_y^n maximum radius of curvature of the logarithmic spiral of the current failure mechanism.

r_y^o maximum radius of curvature of the old (previous failure) logarithmic spiral.

s slope gradient.

t time.

t_μ micromechanical tensile strength.

u displacement vector.

v, v_D, v_k velocities.

x^n minimum angle of the logarithmic spiral of the current failure mechanism.

x^o minimum angle of the old (previous failure) logarithmic spiral.

y^n maximum angle of the logarithmic spiral of the current failure mechanism.

y^o maximum angle of the old (previous failure) logarithmic spiral.

A area.

$A^n, A_1^n, A_2^n, A_3^n,$ areas of the regions defined by *Utili*
A^o, A_1^o, A_2^o, A_3^o *and Crosta* [2011, Figure 3b].

C time scaling constant factor for DEM simulations.

CR crest retreat.

D damage index.

$F^n, F_1^n, F_2^n, F_3^n,$ gravity forces acting on the correspond-
F^o, F_1^o, F_2^o, F_3^o ing regions A^n, etc.

F_k generic force on a particle.

F^N normal contact force between two particles.

F^S shear contact force between two particles.

G gravity center.

H height of full slope.

L^n, L^o lengths defined by *Utili and Crosta* [2011, Figure 3b].

N_S stability number.

X horizontal Cartesian coordinate; axes origin at the initial slope toe.

Y vertical Cartesian coordinate; axes origin at the initial slope toe.

W work.

$\dot{W}^n, \dot{W}_1^n, \dot{W}_2^n, \dot{W}_3^n,$ external work rates done by the corre-
$\dot{W}^o, \dot{W}_1^o, \dot{W}_2^o, \dot{W}_3^o$ sponding regions A^n, etc.

References

Andrews, D. J., and T. C. Hanks (1985), Scarp degraded by linear diffusion: inverse solution for age, *J. Geophys. Res.*, *90*, 10,193–10,208, doi:10.1029/JB090iB12p10193.

Bakker, J. P., and J. W. N. Le Heux (1946), Projective-geometric treatment of O. Lehmann's theory of the transformation of steep mountain slopes, *Proc. K. Ned. Akad. Wet.*, *49*, 533–547.

Bakker, J. P., and J. W. N. Le Heux (1952), A remarkable new geomorphological law, *Proc. K. Ned. Akad. Wet., Ser. B*, *55*, 399–410, 554–571.

Balmforth, N. J., and R. R. Kerswell (2005), Granular collapse in two dimensions, *J. Fluid Mech.*, *538*, 399–428, doi:10.1017/S0022112005005537.

Bell, M., P. J. Fowler, and S. Hillson (Eds.) (1996), *The Experimental Earthwork Project 1960–1992*, Counc. for Br. Archaeol., York, U. K.

Calvetti, F., and R. Nova (2004), Micromechanical approach to slope stability analysis, in *Degradation and Instabilities of Geomaterials*, *CISM Courses Lecutres*, vol. 461, edited by F. Darve and I. Vardoulakis, pp. 235–254, Springer, Berlin.

Calvetti, F., G. B. Crosta, and M. Tatarella (2000), Numerical simulation of dry granular flows: From the reproduction of small-scale experiments to the prediction of rock avalanches, *Riv. Ital. Geotecnica*, *34*, 21–38.

Carson, M. A., and M. J. Kirkby (1972), *Hillslope Form and Process*, 475 pp., Cambridge Univ. Press, Cambridge, U. K.

Crosta, G. B., S. Imposimato, and D. Roddeman (2009), Numerical modeling of 2-D granular step collapse on erodible and nonerodible surface, *J. Geophys. Res.*, *114*, F03020, doi:10.1029/2008JF001186.

Cundall, P. A. (1987), Distinct element models of rock and soil structure, in *Analytical and Computational Methods in Engineering Rock Mechanics*, edited by E. T. Brown, pp. 129–163, Allen and Unwin, London.

Cundall, P., and O. D. L. Strack (1979), Discrete numerical model for granular assemblies, *Geotechnique*, *29*, 47–65, doi:10.1680/geot.1979.29.1.47.

Dixon, J. C., and C. E. Thorn (2005), Chemical weathering and landscape development in mid-latitude alpine environments, *Geomorphology*, *67*, 127–145, doi:10.1016/j.geomorph.2004.07.009.

Estrada, N., A. Taboada, and F. Radjaï (2008), Shear strength and force transmission in granular media with rolling resistance, *Phys. Rev. E*, *78*, 021301, doi:10.1103/PhysRevE.78.021301.

Fisher, O. (1866), On the disintegration of a chalk cliff, *Geol. Mag.*, *3*, 354–356, doi:10.1017/S0016756800167573.

Gough, B. (2010) Investigation into the retrogression of slopes by the Discrete Element Method, M.S. thesis, Oxford Univ., Oxford, U. K.

Heimsath, A. M., W. E. Dietrich, K. Nishiizumi, and R. C. Finkel (1997), The soil production function and landscape equilibrium, *Nature*, *388*, 358–361, doi:10.1038/41056.

Hutchinson, J. N. (1998), A small-scale field check on the Fisher-Lehmann and Bakker–Le Heux cliff degradation models, *Earth Surf. Process. Landf.*, *23*, 913–926, doi:10.1002/(SICI)1096-9837(199810)23:10<913::AID-ESP911>3.0.CO;2-G.

Hutchinson, J. N. (2001), Reading the ground: Morphology and geology in site appraisal, *Q. J. Eng. Geol. Hydrogeol.*, *34*, 7–50, doi:10.1144/qjegh.34.1.7.

Hutchinson, J. N., and J. T. Stuart (2003), Analyses of the morphological changes with time, through denudation and siltation, in ditches of trapezoidal and triangular section, *J. Archaeol. Sci.*, *30*, 797–808.

Jewell, P. A. (1963), *The Experimental Earthwork on Overton Down, Wiltshire 1960*, Br. Assoc. for the Adv. of Sci., London.

Jiang, M. J., H. B. Yan, H. H. Zhu, and S. Utili (2010), Modeling shear behavior and strain localization in cemented sands by two-dimensional distinct element method analyses, *Comput. Geotech.*, *38*, 14–29, doi:10.1016/j.compgeo.2010.09.001.

Kirkby, M. J. (1987), General models of long-term slope evolution through mass movement, in *Slope Stability*, edited by M. G. Anderson and K. S. Richards, pp. 359–379, John Wiley, New York.

Kirkby, M. J., and I. Statham (1975), Surface stone movement and scree formation, *J. Geol.*, *83*, 349–362, doi:10.1086/628097.

Lacaze, L., J. C. Phillips, and R. R. Kerswell (2008), Planar collapse of a granular column: Experiments and discrete element simulations, *Phys. Fluids*, *20*, 063302, doi:10.1063/1.2929375.

Lajeunesse, E., A. Mangeney-Castelnau, and J. P. Vilotte (2004), Spreading of a granular mass on a horizontal plane, *Phys. Fluids*, *16*, 2371, doi:10.1063/1.1736641.

Lehmann, O. (1933), Morphologische Theorie der Verwitterung von SteinschlagwÄanden, *Vierteljahresschr. Naturforsch. Ges. Zurich*, *78*, 83–126.

Lube, G., H. Huppert, S. Sparks, and M. Hallworth (2004), Axisymmetric collapse of granular columns, *J. Fluid Mech.*, *508*, 175–199, doi:10.1017/S0022112004009036.

Lube, G., H. Huppert, S. Sparks, and A. Freundt (2005), Collapses of two-dimensional granular columns, *Phys. Rev. E*, *72*, 041301, doi:10.1103/PhysRevE.72.041301.

Nash, D. B. (1981), Fault: A FORTRAN program for modeling the degradation of active normal fault scarp, *Comput. Geosci.*, *7*(3), 249–266, doi:10.1016/0098-3004(81)90047-9.

Ng, T. T., and R. Dobry (1994), Numerical simulations of monotonic and cyclic loading of granular soil, *J. Geotech. Geoenviron. Eng.*, *120*, 388–403.

Nova, R. (2008), *Meccanica delle Costruzioni Geotecniche (in Italian)*, Cittastudi, Milan, Italy.

Obanawa, H., and Y. Matsukura (2006), Mathematical modelling of talus development, *Comput. Geosci.*, *32*, 1461–1478, doi:10.1016/j.cageo.2006.05.004.

Potts, D. M., N. Kovacevic, and P. R. Vaughan (1997), Delayed collapse of cut slopes in stiff clay, *Geotechnique*, *47*, 953–982, doi:10.1680/geot.1997.47.5.953.

Radenkovic, D. (1961), Théorie des charges limites: Extension à la mécanique des sols, *Publ. Sci. Tech. Minist. Air (Fr.)*, *116*.

Scheidegger, A. E. (1961), Mathematical models of slope development, *Geol. Soc. Am. Bull.*, *72*, 37–50, doi:10.1130/0016-7606(1961)72[37:MMOSD]2.0.CO;2.

Schumm, S. A. (1956), The role of creep and rainwash on the retreat of badland slopes, *Am. J. Sci.*, *254*, 693–706, doi:10.2475/ajs.254.11.693.

Siavoshi, S., and A. Kudrolli (2005), Failure of a granular step, *Phys. Rev. E*, *71*, 051302, doi:10.1103/PhysRevE.71.051302.

Taboada, A., and N. Estrada (2009), Rock-and-soil avalanches: Theory and simulation, *J. Geophys. Res.*, *114*, F03004, doi:10.1029/2008JF001072.

Taboada, A., N. Estrada, and F. Radjai (2006), Additive decomposition of shear strength in cohesive granular media from grain-scale interactions, *Phys. Rev. Lett.*, *97*, 098302–098306, doi:10.1103/PhysRevLett.97.098302.

Troncone, A. (2005), Numerical analysis of a landslide in soils with strain-softening behaviour, *Geotechnique*, *55*, 585–596, doi:10.1680/geot.2005.55.8.585.

Utili, S. (2006), Evolution of natural slopes subject to weathering: An analytical and numerical study, Ph.D thesis, Politecnico di Milano, Milan, Italy.

Utili, S., and G. B. Crosta (2011), Modeling the evolution of natural cliffs subject to weathering: 1. Limit analysis approach, *J. Geophys. Res.*, *116*, F01017, doi:10.1029/2009JF001557.

Utili, S., and R. Nova (2008), DEM analysis of bonded granular geo-materials, *Int. J. Numer. Anal. Methods Geomech.*, *32*, 1997–2031, doi:10.1002/nag.728.

Wang, Y. H., and S. C. Leung (2008), A particulate scale investigation of cemented sand behaviour, *Can. Geotech. J.*, *45*, 29–44, doi:10.1139/T07-070.

Young, A. (1972), *Slopes*, 268 pp., Longman, London.

Zheng, H., D. F. Liu, and C. G. Li (2005), Slope stability analysis based on elasto-plastic finite element method, *Int. J. Numer. Methods Eng.*, *64*, 1871–1888, doi:10.1002/nme.1406.

G. B. Crosta, Dipartimento di Scienze Geologiche e Geotecnologie, Università degli Studi di Milano-Bicocca, Piazza della Scienza 4, Milano I-20126, Italy.

S. Utili, Department of Engineering Science, University of Oxford, Parks Road, Jenkin Bldg., Rm. 21, Oxford OX1 3PJ, UK. (stefano.utili@eng.ox.ac.uk)